Optics Letters

# Crawling wave optical coherence elastography

Panomsak Meemon,[1,2,*] Jianing Yao,[1] Ying-Ju Chu,[3] Fernando Zvietcovich,[4] Kevin J. Parker,[3,4] and Jannick P. Rolland[1,3]

[1]The Institute of Optics, University of Rochester, Rochester, New York 14627, USA
[2]School of Physics, Institute of Science, Suranaree University of Technology, Nakhon Ratchasima 30000, Thailand
[3]Department of Biomedical Engineering, University of Rochester, Rochester, New York 14627, USA
[4]Department of Electrical and Computer Engineering, University of Rochester, Rochester, New York 14627, USA
*Corresponding author: panomsak@sut.ac.th

Received 30 September 2015; accepted 29 December 2015; posted 8 January 2016 (Doc. ID 251033); published 17 February 2016

**Elastography is a technique that measures and maps the local elastic property of biological tissues. Aiming for detection of micron-scale inclusions, various optical elastography, especially optical coherence elastography (OCE), techniques have been investigated over the past decade. The challenges of current optical elastography methods include the decrease in elastographic resolution as compared with its parent imaging resolution, the detection sensitivity and accuracy, and the cost of the overall system. Here we report for the first time, we believe, on an elastography technique—crawling wave optical coherence elastography (CRW-OCE)—which significantly lowers the requirements on the imaging speed and opens the path to high-resolution and high-sensitivity OCE at relatively low cost. Methods of crawling wave excitation, data acquisition, and crawling wave tracking are presented.** 

***OCIS codes:*** (110.4500) Optical coherence tomography; (100.2960) Image analysis; (120.7280) Vibration analysis.

http://dx.doi.org/10.1364/OL.41.000847

Towards early diagnostic and treatment, methods to quantify and localize tissue stiffness with high sensitivity are sought. Elastography is one such method for quantifying the local stiffness or elastic properties of tissues through an imaging technique, e.g., ultrasound imaging (USI), magnetic resonance imaging (MRI), or optical imaging [1, 2] in order to detect or classify tumors. Elastography quantifies the local displacements of individual tissue elements from data acquired by a chosen imaging modality, while introducing forces on them. The local displacements serve as the basis to estimate the local elasticity of the sample that may be mapped as an image called an elastogram [3]. Over decades, various techniques of elastography have been developed and proposed, utilizing different imaging modalities, excitation forces, detection methods, and contrast mappings [1,2].

While ultrasound elastography works well for the detection of large size stiffness on the order of centimeters, the detection of small size inclusions is limited by the resolution. Optical imaging, particularly optical coherence tomography (OCT) [4], provides higher resolution as compared with USI. The drawback of OCT compared to USI and MRI is the depth penetration limit, which is about 2–3 mm in biological tissues. Nevertheless, the high resolution of OCT may enable elastography of small-size inclusions, such as skin cancers.

Static-loading OCE was first demonstrated by Schmitt in 1998 [5]. Subsequently, different methods of static compressional excitations and processing algorithms were proposed by other groups of researchers [6–8]. Over the years, several techniques and experimental setups of static-loading OCE and dynamic-loading OCE have been reported. For instance, Wang *et al.* demonstrated the use of Doppler OCT to detect the vibration amplitude of a mechanical wave within a tissue phantom under harmonic mechanical excitation introduced by a translation stage [9]; Kennedy *et al.* introduced the use of a ring actuator as an excitation source in vibrational-loading OCE. The ability to both excite and image the sample from the same direction is promising for elastography of *in vivo* biological samples [10]. Furthermore, Liang *et al.* reported an investigation of the strain contrast introduced by different excitation frequencies driven by a piezoelectric actuator. A strain map of an *ex vivo* rat tumor was demonstrated [11]. Manapuram *et al.* recently reported on the use of phase-stabilized swept-source OCT to study the response of the shear vibrational wave to an impulse excitation at the surface of gelatin phantoms of different concentrations. The shear velocity and amplitude attenuation of the response were measured and analyzed [12]. Several methods of noncontact excitation were also investigated and proposed, which opens the path for *in vivo* application of vibration-amplitude OCE [13]. A thorough review on various techniques of OCE was recently presented in [2].

All of the previous works on vibration OCE determined the local elasticity of samples based on direct measurement of either the amplitude and/or the velocity of the propagating shear vibrational wave. Given the absolute velocity of the shear wave in a medium on the order of 2–4 m/s, the wave propagates considerably fast if attempted to be captured within the typical field of view (FOV) of OCT, which commonly spans millimeters to tens of millimeters. As a result, high-speed phase-sensitive OCT is typically essential to obtain accurate results. An alternative approach is to determine the shear wave speed

inside a medium by characterizing the interference patterns between two shear waves, a technique that was first introduced in ultrasound elastography by Wu *et al.* [14]. When the frequencies of the two vibration sources are the same, the static interference pattern can be observed. Furthermore, by introducing a slightly different frequency to one of the vibrational sources, a slowly moving interference pattern is generated, a so-called "crawling wave" interference pattern. The local speed of the crawling wave may be measured, and the velocity of the local shear wave may then be computed as

$$v_{\text{shear}}(x) = (2\omega/\Delta\omega)v_{\text{crawl}}(x), \quad (1)$$

where $\omega$ is the vibration frequency of the shaker and $\Delta\omega$ is the frequency difference between the two sources [15]. Sequentially, the elastogram of the sample may be produced from the relation between the local shear velocity and local shear modulus as $\mu(x) = \rho v_{\text{shear}}^2(x)$, where $\rho$ is the density of the material [2]. In addition, for incompressible material, the relation between the shear modulus and the Young's modulus becomes $E \approx 3\mu$. Therefore, the local speed of the crawling wave can directly be used to create an elastogram of the sample.

In this Letter, we demonstrate for the first time, to the best of our knowledge, a crawling wave captured with optical coherence elastography (CRW-OCE). The experimental setup of crawling wave excitation is presented, and a technique of tracking the crawling wave using phase-resolved Doppler OCT is demonstrated. For validation of the proposed technique, we computed the local shear velocity from the measured crawling wave velocity using Eq. (1) and compared the results with those obtained from a standard stress relaxation test. A cross-sectional elastogram of a sample generated from the local shear velocity is revealed.

Our experimental setup implements crawling wave excitation and detection as illustrated in Fig. 1. The imaging system utilizes a swept source (HSL-2100-WR, Santec) with a center wavelength of 1318 nm and a FWHM bandwidth of 125 nm. The maximum sensitivity of the system was 112 dB, as measured in [16]. The depth of imaging of the system was limited by the spectral resolution of the laser source and was measured to be 5 mm, as determined by the depth location of the −10 dB sensitivity fall-off. The optical lateral resolution was quantified to be approximately 20 μm. The FWHM of the axial point-spread function of the system after dispersion compensation was measured to be 10 μm. The algorithm for extracting Doppler maps from swept-source OCT data was previously detailed in [17,18].

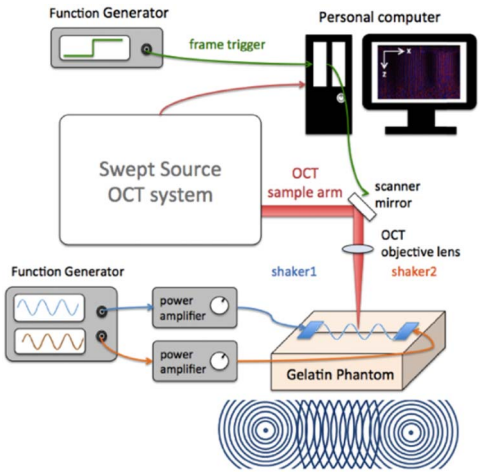


**Fig. 1.** Simplified schematic of the custom-built crawling wave optical coherence elastography (CRW-OCE) microscope.

Throughout our experiments, gelatin phantoms with varied concentrations of gelatin within a matrix were constructed to mimic soft tissues with different stiffnesses. Varying the relative amount of gelatin modified the phantom's elastic properties. As for the optical properties, the refractive index of the phantom was approximately 1.35 [19], which is close to that of most tissues. In addition, gelatin phantoms have the advantage of being adjustable to yield scattering and absorption properties by adding a scattering agent like $TiO_2$ and intralipid, and absorbing elements like India ink, or any dye of interest, respectively [19]. For our experiments, we added coffee creamer to the phantom to enhance its scattering property. Milk powder or coffee creamer are lipid-based microparticles that work well as optical scatterers in tissue-simulating phantoms. They also provide a refractive index similar to that of soft tissue, with a particle size on the order of 100 nm [20]. When intralipid is added to the gelatin matrix, the resulting scattering coefficient of the phantom has a linear dependency on the intralipid concentration, and as such, the effective penetration depth of the system decreases accordingly and in a linear fashion. Considering the wavelength dependency of the scattering coefficients, the penetration depth of the swept-source laser used in our experiment was limited to about 2.5 mm in the presence of 2% intralipid [21].

Using the setup illustrated in Fig. 1, we introduced a vibrational shear wave interference pattern within the gelatin phantom by using two piezoelectric actuators (APC 40-2020, APC International, Ltd.) connected to stereo amplifiers (LP-2020A +, Lepai) that amplified sinusoidal waveforms from a dual channel function generator (AFG320, Tektronix). The two shakers vibrated perpendicular to the surface of the phantom and were placed in the same lateral scanning plane as that of the OCT data acquisition, with at least 8 cm separation. The focusing beam from the OCT imaging objective lens was located around the midpoint between the two shakers. When the excitation frequencies of the two shakers are set to be the same, a standing interference pattern between the two shear waves occurs. To maximize the contrast of the detected interference pattern, the vibration amplitude of each shaker was adjusted to provide a similar Doppler contrast. This was done by turning on only one shaker at a time and observing the Doppler image in real time while adjusting the applied voltage to the shaker. A crawling wave pattern was then introduced by slightly increasing the excitation frequency of one of the shakers in the range of 0.1–2 Hz. To capture the propagation of the crawling wave, several Doppler cross-sectional images were sequentially taken. By tracking the local velocity of the crawling wave, we determined the local shear velocity and hence the local shear modulus or local stiffness of the sample.

From our experiment, we found that there are advantages to using the crawling wave excitation in OCE. First, the two opposing sources and their interfering wavefronts produce a relatively uniform, high contrast and high signal-to-noise ratio (SNR) displacement field across the FOV, as compared to a single source, which exhibits nonuniform vibration amplitude caused by damped vibration characteristics.

Second, as stated in Eq. (1), the crawling wave travels across the OCT imaging FOV at much slower speed than the shear

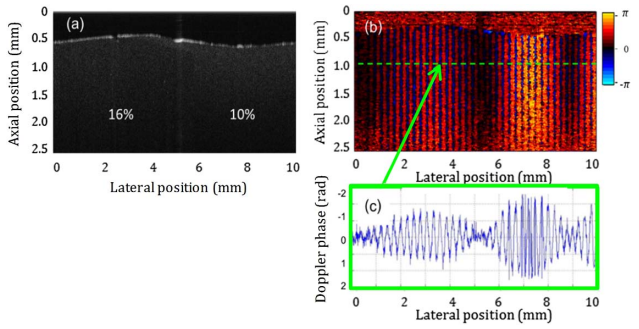


**Fig. 2.** (a) An example of an OCT cross-sectional intensity map of a two-sided gelatin phantom. (b) Doppler image of the phantom obtained at the same region as in (a). A time lapse of the Doppler map in (b) is provided in supplementary Visualization 1. (c) An example of a lateral profile at about 1 mm depth in the Doppler image in (b).

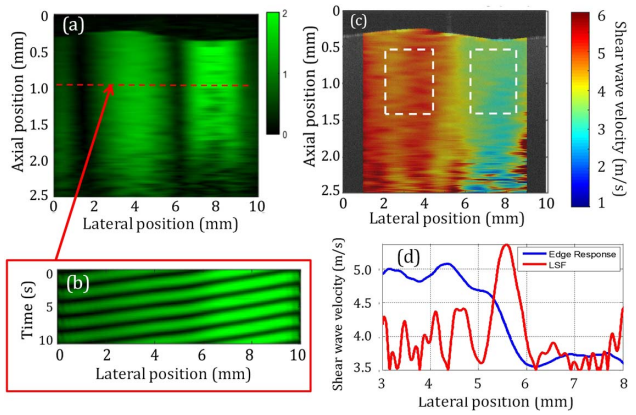


**Fig. 3.** (a) A cross-sectional map of the crawling wave amplitude of the captured Doppler map in Fig. 2(b) (see Visualization 2). (b) An example of a space-time mapping of the envelope data in (a) constructed at about 1 mm depth. (c) By analyzing the space-time maps in (b), a cross-sectional shear velocity map was obtained, which serves as a CRW-OCE elastogram that clearly distinguishes the two regions of the phantom. (d) An edge response and LSF were computed at around 1 mm depth of the elastogram in (c).

wave itself. In addition, for any given excited shear wave frequency, the speed of the crawling wave is fully controllable via the adjustment of the frequency difference $\Delta\omega$. This unique capability allows for the determination of the local shear velocity, and hence, the shear modulus of a sample at slower detection speed without losing the detection sensitivity and resolution. Therefore, the proposed CRW-OCE opens up the potential for improvement in the detection efficiency as well as enabling cost reduction in the overall optical elastography system.

To validate the ability of CRW-OCE to differentiate stiffness, we fabricated a two-sided gelatin phantom having two different elasticities achieved by setting different gelatin concentrations (i.e., 16% and 10% gelatin). Each side, however, had similar scattering properties, since the same concentration of intralipid powder was used. A conventional OCT cross-sectional image of the phantom acquired in a region around the boundary of the two-sides is shown in Fig. 2(a), where the two regions of the phantom exhibit similar scattering contrast, as expected. To observe the propagation of the crawling wave across the boundary between the two regions, we acquired multiple frames of B-mode Doppler at the frame duration of 200 ms (i.e., 5 frames per second). Each frame of Doppler image consisted of 1500 axial scans (A-scans), covering a 10 mm lateral distance sampled at every 7 μm. Each A-scan of the Doppler map was obtained by computing the phase difference with its adjacent A-scan along the lateral direction by using the same algorithm presented in [17]. To generate an observable crawling wave across the specific lateral FOV, an excitation frequency of 500 Hz with the frequency difference of 0.5 Hz was chosen, which introduced 2–3 cycles of a crawling wave across the 10 mm lateral FOV. An example of the captured Doppler image is demonstrated in Fig. 2(b), while the propagation of the crawling wave is shown in a supplementary Visualization 1. Figure 2(c) shows a lateral profile of the Doppler phase in Fig. 2(b) at the depth of about 1 mm from the surface.

The detected Doppler signals shown in Figs. 2(b) and 2(c) consist of two signals. The fast varying signal (dense alternate red and blue stripes) is a temporal vibration of the shear wave, which corresponds to the frequency of the shaker. The crawling wave corresponds to the slow-varying envelope of the signal shown in Fig. 2(c). The frequency of the fast variation of the Doppler phase can be considered as a carrier signal, whose frequency can be accurately computed from the excitation frequency (i.e., 500 Hz). Therefore, the crawling envelope shown in Fig. 3(a) can be extracted by utilizing this known modulation frequency. The envelope tracking was performed for every lateral profile of the 3D dataset of Doppler images, covering 10 mm lateral distance and 2.5 mm depth, and acquired over 10-second time intervals as demonstrated in a supplementary Visualization 2. From the extracted envelope dataset, direct observation of the crawling wave propagation was enabled by constructing a space-time map at a specific depth location as shown in Fig. 3(b). The slope in the space-time map directly represents the inverse of the crawling wave speed, which also relates to the shear wave speed through Eq. (1). Using the data presented in Fig. 3(a), the local shear wave velocity $v_{\text{shear}}(x)$ was computed by adapting the phase derivative method presented in [22]. First, the initial phase $\theta(x)$ of each column of the space-time map was determined. Then, by taking the derivative of $\theta(x)$, the shear wave velocity $v_{\text{shear}}(x)$ was calculated by

$$v_{\text{shear}}(x) = \frac{\omega}{\theta'(x)} \approx \frac{\omega \Delta x}{\Delta\theta(x)}, \tag{2}$$

where $\omega$ is the excitation frequency. A depth cross-sectional elastogram was generated from the computed $v_{\text{shear}}(x)$ across the 2.5 mm depth as shown in Fig. 3(c). We used 50 frames of Doppler cross-sectional images to produce an elastogram, which corresponds to an acquisition time of about 10 s. This amount of data was verified to give a fair estimation of the phase $\theta(x)$ and hence the phase difference $\Delta\theta(x)$. A trade-off exists between acquisition speed and the estimation accuracy of phase that will then affect the performance of the phase derivative computation. We have established that an elastogram may be generated in as fast as a couple of seconds if the task is to differentiate tissues as opposed to estimate elasticity value.

To validate the CRW-OCE measurement, small portions of both the 10% and 16% gelatin phantoms were extracted ($N = 3$), shaped into cylindrical shapes, and put under the mechanical stress relaxation test.

A precise electromechanical control of the load was applied to the phantom using the MTS Q-Test/5 Universal Testing Machine. The obtained stress relaxation test response was then fit to the modified fractional derivative-standard linear solid (SLS) model [23], and hence, the viscoelastic coefficients of the sample were estimated. The shear wave velocity at excitation frequency of 500 Hz was then estimated. For the chosen 500 Hz excitation frequency, the shear wave velocities reconstructed by the mechanical tests for the 10% and 16% gelatin phantoms were $3.18 \pm 0.06$ m/s and $4.80 \pm 0.07$ m/s, respectively. Estimated from the shear velocity map in Fig. 3(c), the average shear velocity of the 10% and 16% gelatin phantoms were computed within the regions approximately marked by white dash boxes to be $3.49 \pm 0.15$ m/s and $4.86 \pm 0.19$ m/s, respectively. The measured speed of the crawling wave is in agreement with the standard stress relaxation test results with less than 10% error for both concentrations of gelatin.

In conclusion, we have demonstrated the implementation and validation of CRW-OCE. In ultrasound Doppler, the imaging FOV is large, and hence it is possible to measure directly the wavelength of the crawling wave that typically is in the order of tens of millimeters. In CRW-OCE, however, the FOV is comparably small, and only a few cycles of the crawling wave can be observed in a single Doppler frame. As a result, it is not practical to determine the crawling speed from its directly measured wavelength, and hence, the static shear wave interference method is not suitable. Nevertheless, the high resolution and high speed imaging capability of OCT allows for direct tracking of the local speed of the crawling pattern as it propagates across the imaging FOV over a period of time.

By performing the analysis on multiple frames of cross-sectional images continuously captured by the phase-resolved Doppler OCT system, we computed the speed of the crawling wave and used it to estimate the shear velocity of the local vibrational wave, which is directly related to the local stiffness of the sample. Even though the final elastogram consists of almost the same number of lateral samples as compared to its parent OCT image, its elastographic resolution is expected to be poorer due to the use of a smoothing filter. As an attempt to estimate the resolution of the current implementation of our CRW-OCE, using the data in Fig. 3(c), an edge response was computed by averaging lateral profiles at the boundary between the two sides of gelatin phantom, as shown by the blue plot in Fig. 3(d). The first derivative of the edge response yields a line spread function (LSF) [24], as shown by the red plot in Fig. 3(d). The resolution of the CRW-OCE was estimated by measuring the FWHM of the LSF to be about 0.56 mm. This number only provides a rough approximation since the phantom may not exhibit a perfect step contrast and hence may only represent an estimate of the resolution of the CRW-OCE.

The measured speed of the crawling wave is shown to be in good agreement with the standard stress relaxation test results, given the numerous sources of errors influencing the phase velocity estimates (noise and reflections), separately, the mechanical measurements (room temperature changes, imperfection of the cylindrical shapes), and finally, the inherent limitations of the fractional derivative-SLS model used to extrapolate from stress relaxation the shear wave velocity at 500 Hz. The crawling wave elastography technique allows for the shear velocity measurement at much slower detection speed. This property resulted in simplifications to the system design and tracking algorithm. The advantage of using OCT as the detection method lies in its ability to achieve high resolution and sensitivity, which could open the path for detection of micron-size pathological tissues.

**Funding.** II-VI foundation, (058166-002); Higher Education Research Promotion and National Research University Project of Thailand, Office of the Higher Education Commission.

## REFERENCES

1. K. Parker, M. Doyley, and D. Rubens, Phys. Med. Biol. **56**, R1 (2011).
2. B. F. Kennedy, K. M. Kennedy, and D. D. Sampson, IEEE J. Sel. Top. Quantum Electron. **20**, 272 (2014).
3. J. Ophir, I. Cespedes, H. Ponnekanti, Y. Yazdi, and X. Li, Ultrason. Im. **13**, 111 (1991).
4. D. Huang, E. A. Swanson, C. P. Lin, J. S. Schuman, W. G. Stinson, W. Chang, M. R. Hee, T. Flotte, K. Gregory, C. A. Puliafito, and J. G. Fujimoto, Science **254**, 1178 (1991).
5. J. Schmitt, Opt. Express **3**, 199 (1998).
6. B. F. Kennedy, R. A. McLaughlin, K. M. Kennedy, L. Chin, A. Curatolo, A. Tien, B. Latham, C. M. Saunders, and D. D. Sampson, Biomed. Opt. Express **5**, 2113 (2014).
7. A. Nahas, M. Bauer, S. Roux, and A. C. Boccara, Biomed. Opt. Express **4**, 2138 (2013).
8. J. Rogowska, N. A. Patel, J. G. Fujimoto, and M. E. Brezinski, Heart (London, U. K.) **90**, 556 (2004).
9. R. K. Wang, Z. Ma, and S. Kirkpatrick, Appl. Phys. Lett. **89**, 144103 (2006).
10. B. F. Kennedy, T. R. Hillman, R. A. McLaughlin, B. C. Quirk, and D. D. Sampson, Opt. Express **17**, 21762 (2009).
11. X. Liang, S. G. Adie, R. John, and S. A. Boppart, Opt. Express **18**, 14183 (2010).
12. R. K. Manapuram, S. Aglyamov, F. Menodiado, M. Mashiatulla, S. Wang, S. Baranov, J. Li, S. Emelianov, and K. Larin, Laser Phys. **22**, 1439 (2012).
13. S. Wang, J. Li, R. K. Manapuram, F. M. Menodiado, D. R. Ingram, M. D. Twa, A. J. Lazar, D. C. Lev, R. E. Pollock, and K. V. Larin, Opt. Lett. **37**, 5184 (2012).
14. Z. Wu, K. Hoyt, D. J. Rubens, and K. J. Parker, J. Acoust. Soc. Am. **120**, 535 (2006).
15. Z. Wu, L. S. Taylor, D. J. Rubens, and K. J. Parker, Phys. Med. Biol. **49**, 911 (2004).
16. J. Yao, P. Meemon, M. Ponting, and J. P. Rolland, Opt. Express **23**, 6428 (2015).
17. P. Meemon, J. Yao, K.-S. Lee, K. P. Thompson, M. Ponting, E. Baer, and J. P. Rolland, Sci. Rep. **3**, 1709 (2013).
18. P. Meemon, K. S. Lee, and J. P. Rolland, Biomed. Opt. Express **1**, 537 (2010).
19. H. G. Akarçay, S. Preisser, M. Frenz, and J. Rička, Biomed. Opt. Express **3**, 418 (2012).
20. P. Lai, X. Xu, and L. V. Wang, J. Biomed. Opt. **19**, 035002 (2014).
21. V. Kodach, J. Kalkman, D. Faber, and T. Van Leeuwen, Biomed. Opt. Express **1**, 176 (2010).
22. Z. Hah, C. Hazard, B. Mills, C. Barry, D. Rubens, and K. Parker, Ultrasound Med. Biol. **38**, 312 (2012).
23. D. Craiem, F. Rojo, J. Atienza, G. Guinea, and R. L. Armentano, Latin Am. Appl. Res. **38**, 141 (2008).
24. G. D. Boreman, *Handbook of Optics*, 3rd ed., Vol. **1** of Geometrical and Physical Optics, Polarized Light, Components and Instruments (Optical Society of America, 2010), Chap. 4, p. 4–7.